Performance Evaluation for Multi-arm Manipulation of Hollow Suspended Organs

Wei Wei, *Student Member, IEEE*, Roger E. Goldman, Howard F. Fine, Stanley Chang, and Nabil Simaan, *Member, IEEE*

***Abstract*—This paper presents a unified mathematical framework for modeling and evaluating the performance of multiple robotic arms that operate on hollow suspended organs. This framework is applied to a novel two-armed hybrid robotic system being developed for ophthalmic vitreous surgeries. Four cases are designated to capture the general movements required for any surgical procedure associated with hollow suspended organs. Dexterity measures, based on multiple characteristic lengths, are presented for procedures corresponding to these manipulation cases. Simulation results of the dual-arm robotic system for ophthalmic surgery are presented for all four manipulation cases. A comparison of this robotic system with current surgical tools shows a significant improvement in intraocular dexterity.**

***Index Terms*—Dexterity, hybrid robots, medical robotics, multiple-arm manipulation, ophthalmic surgery.**

I. Introduction

DUE to the micron scale and delicacy of retinal tissues, only highly experienced ophthalmic surgeons can successfully perform these demanding, yet common, procedures. Robot-assisted ophthalmic surgery has been proposed to address this challenge. Grace [1] presented a miniature telesurgical parallel robot for the treatment of retinal venous occlusion in ophthalmic surgery. Das *et al*. [2] and Charles *et al*. [3] developed robot assisted micro surgery (RAMS) workstation, which is a cable-driven master/slave telerobotic system. Ang *et al*. [4] developed a hand-held microsurgical instrument for vitreoretinal microsurgery via tremor canceling. Taylor *et al*. and Kumar *et al*. [5], [6] presented a cooperative manipulation robot for microsurgical applications. Ikuta and Kato [7] designed a hand-held forceps with an active joint and fiberscope to address the lack of dexterity inside the eye.

Previous works addressed major challenges of statistically characterizing hand tremor [8], [9], providing active tremor cancellation [4], high precision [1], [2], [6], and force monitoring in eye surgery [10]. However, the surgical need to manipulate several instruments with high precision in the vitreous body, while stabilizing or manipulating the eye under the microscope presents a novel integrated challenge. This need led to our recent paper [11] and ongoing development of a robotic system that is capable of intraocular and orbital manipulations of the eye (see Fig. 1).

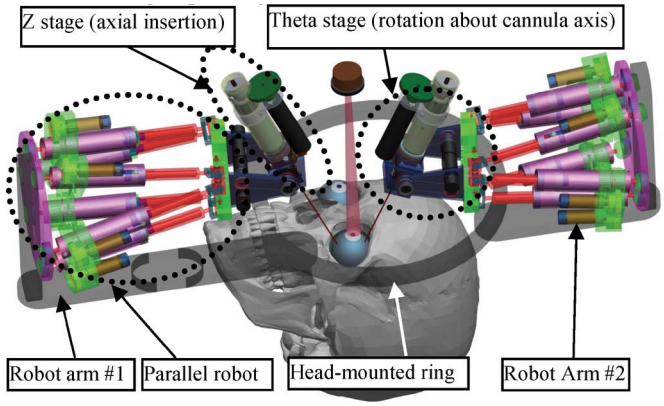

Fig. 1. Proposed dual-arm robotic system for orbital and intraocular dexterity.

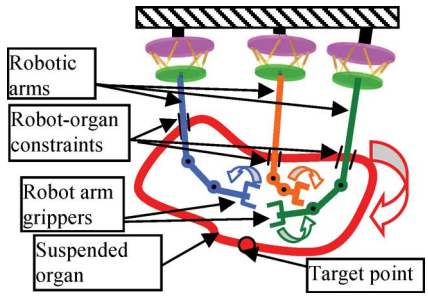

Fig. 2. Multi-armed manipulation and operation inside a hollow suspended organ.

The problem of stabilizing the eye while manipulating structures within [11] can be generalized to any operation on hollow organs with a stability not guaranteed by anatomic constraints, e.g., eye, stomach, bladder, etc., as illustrated in Fig. 2. The suspended organ is manipulated and stabilized using several robotic arms that are inserted into the organ. The literature addresses the modeling and evaluation of constrained multibody system [12]–[15] and multifingered hands [16]–[18]. However, these mathematical models cannot be directly applied to systems, as in Fig. 2, due to assumption in the grasping literature that the stabilizing bodies do not penetrate the grasped object.

Performance evaluation of this system required an updated metric due to its hybrid structure. Although many works have focused on performance measures including manipulability

Manuscript received July 6, 2007; revised January 10, 2008. First published December 2, 2008; current version published February 4, 2009. This paper was recommended for publication by Associate Editor B.-J. Yi and Editor F. Park upon evaluation of the reviewers' comments. The work of W. Wei was supported by the National Science Foundation (NSF) under Engineering Research Center Grant EEC9731478, by the National Institute of Health (NIH) under Grant 1 R21 EB004457-01, and by Columbia University internal funds, and Starting July 2007, he was funded by NSF Grant CBET0651649.

W. Wei, R. E. Goldman, and N. Simaan are with the Department of Mechanical Engineering, Columbia University, New York, NY 10027 USA (e-mail: ww2161@columbia.edu; reg2117@columbia.edu; ns2236@columbia.edu).

H. F. Fine and S. Chang are with the Department of Ophthalmology, Columbia University, New York, NY 10032 USA (e-mail: hff2101@columbia.edu; sc434@columbia.edu).

Color versions of one or more of the figures in this paper are available online at http://ieeexplore.ieee.org.

Digital Object Identifier 10.1109/TRO.2008.2006865

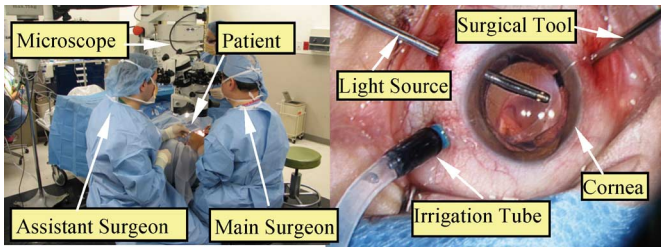

Fig. 3. Typical surgical setup for ophthalmic surgery.

ellipsoids [13], [19], [20], manipulability polytopes [21], [22], isotropy measures [23], [24], kinematic conditioning [25]–[27], and dexterity [28], [29], these metrics do not address the problem of dexterity evaluation for systems with multiple parallel and serial sections. Wang and Chirikjian presented the error propagation problem of hybrid robots in [30]; however, an effective method to evaluate the hybrid robot's performance is still missing. Furthermore, there is no work done to systematically model and evaluate the dexterity of surgical procedures on hollow suspended organs while considering the dexterity in manipulating the organ and operating inside it.

The contributions of this paper are the following. A unified kinematic model is developed to analyze a partially constrained hollow object manipulated by several inserted robotic arms. This model is applicable to robotic assistance on hollow suspended organs, such as the eye. The paper applies this framework to justify the design of a dual-arm telerobotic slave for ophthalmic surgery. This slave is aimed at answering the unaddressed challenge of orbital manipulation and dexterous bi-manual operations inside the eye. Further, our approach adds to existing work on dexterity evaluation of multifingered hands and cooperative manipulation systems by analyzing the constrained motion of a hollow object through four manipulation cases. These cases model the dexterity in manipulating the object and operating inside it via insertion constraints. The paper defines dexterity measures for each of these four cases and identifies the clinical relevance of each case in ophthalmic surgery.

II. Current Surgical Setup for Ophthalmic Surgery

The typical surgical setup for ophthalmic surgery is shown in Fig. 3. Two surgeons coordinate to perform the ophthalmic surgical procedures. The main surgeon sits superior to the patient's head and performs most of the surgical tasks, including manipulation of the surgical instruments and the light source. The assistant surgeon sits beside the patient's head to provide irrigation and removal of fluids and adjust the placement of the external visualization lenses. A second assistant delivers tools and supplies to the surgeons.

Three incisions are typically made in the sclera to provide access to the vitreous body for an irrigation tube, a surgical instrument, and a light source. The light source occasionally performs double duty as a second surgical tool. The irrigation tube injects liquid to maintain intraocular pressure. The light source illuminates the retina for proper visualization under the microscope. The surgical tools, including picks, forceps, vitrectomy cutters, and other laser ablation devices, vary depending on the requirements of the procedure [31]. The surgeons operate using a microscope while visualizing the retina through a dilated iris. Because the visual field does not contain the entire retinal surface, procedures often require tilting the eye under the microscope in order to view peripheral areas of the retina.

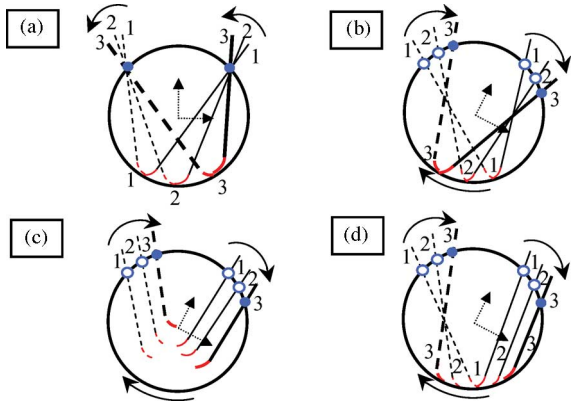

Fig. 4. Kinematic demonstration of the four manipulation cases. Solid lines denote the first arm, while the dotted lines denote the second arm; the thick lines and solid circles denote the final position of the arms and the entry ports.

The repertoire of manipulation tasks in ophthalmic surgical procedures is segmented into four cases of intraocular and orbital manipulations (see Fig. 4). Although Fig. 4 describes these cases with reference to ophthalmic surgery, they are applicable to manipulation of any hollow suspended organ.

Case 1: Intraocular operation with eye stabilization. This case quantifies the ability of the robotic system to perform a specified surgical task inside the eye (Fig. 4(a)).

Case 2: Eye manipulation with constrained intraocular motions. This case evaluates orbital dexterity, a measure of how well the robotic arms can rotate the eye, while respecting kinematic constraints at the incision points and maintaining zero velocity of the forceps relative to the retina (Fig. 4(b)).

Case 3: Eye manipulation with unconstrained intraocular motion. This case evaluates the orbital dexterity without constraint of the forceps relative to the retina (Fig. 4(c)).

Case 4: Simultaneous eye manipulation and intraocular operation. This case measures dexterities of simultaneous intraocular operation and orbital manipulation as the robot rotates the eye and operates inside it (Fig. 4(d)).

The relevance of these cases in ophthalmic surgery is depicted in Figs. 5 and 6. Membrane peeling (Fig. 5(a)) falls into case 1. In this procedure, the eye must be stabilized by the arms while dexterous and precise reach is performed in peeling the micron-thick membrane of scar tissue away from the underlying retina. Fig. 5(a) shows a bi-manual approach for membrane peeling, while Fig. 6(a) shows a forceps used to pull a membrane.

The visualization inside the eye is limited by the dilated iris. The surgeons must tilt the eye under the microscope in order to visualize the peripheral areas of the eye. This movement is performed while steadying the micro-tools inside the eye, and therefore, falls into case 2. Examples shown in Figs. 5(b) and 6(b) illustrate membrane peeling by the ciliary body. This procedure presents challenges in accessing and visualizing the surgical site using straight tools while tilting the eye.

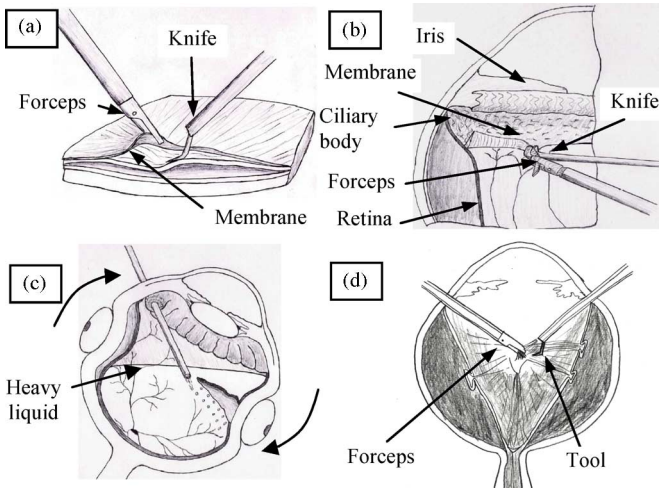

Fig. 5. Illustration of medical procedures corresponding to the four manipulation cases defined in Fig. 4. These figures have been reproduced based on [31] with permission of the American Medical Association (AMA).

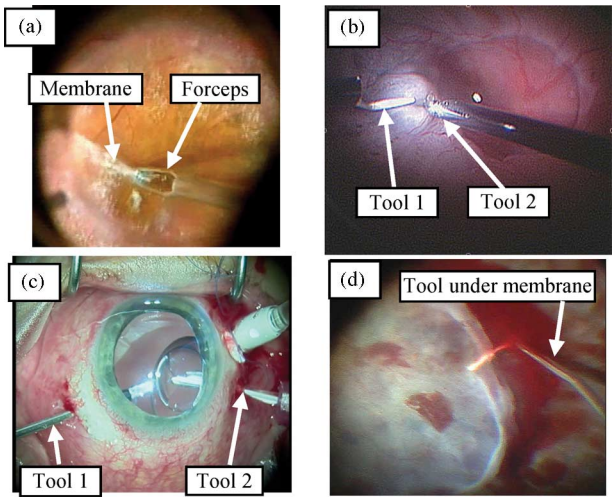

Fig. 6. Intraoperative photographs of procedures that perform analogous maneuvers to cases 1–4 in Fig. 4. (a) Central epiretinal membrane peeling over the macula requires stabilization of the eye while gently peeling thin membranes. (b) Peripheral epiretinal membrane peeling in close proximity to the ciliary body requires tilting of the eye for visualization. (c) Silicone oil is removed by tilting the eye so it floats upward toward the aspirating cannula. (d) Complex dissection of membranes in proliferative vitreoretinopathy requires manipulation of both the eye for visualization and the intraocular tools to perform delicate peeling procedures.

Case 3 is relevant for applications where the manipulation of the eye itself is important, while there is no need for intraocular dexterity. An example of such a procedure includes treatment of retinal detachment using a dense liquid (perfluorocarbon liquid) (Fig. 5(c)). In this procedure, a small incision is made in the detached region to allow aspiration of unwanted fluid between the retina and the retinal pigment epithelium. The eye is then tilted in order to roll the liquid on the surface of the retina. The dense liquid is used to flatten the detached region of the retina. Fig. 6(c) shows the application of removing silicone oil by tilting the eyeball.

Case 4 (Figs. 5(d) and 6(d)) is relevant for operations within the peripheral areas of the eye while having to rotate the eye in order to obtain a better view. In current practice, surgeons retract their tools while tilting the eye and subsequently reposition the tip of the instruments in the surgical site. We plan on using the robot to allow simultaneous tilting and distal intraocular operation in order to decrease the operation time and the number of delicate regrasping operations.

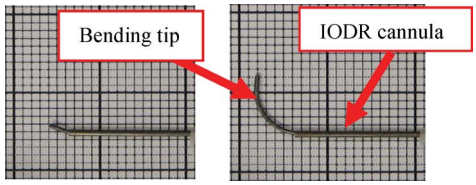

Fig. 7. IODR shown in retracted and open configurations.

The limitations of the current surgical setup include the lack of distal dexterity inside the eye, limited ability to perform precise coordinated bimanual operations, lack of precise stabilization and manipulation of the eye itself under the microscope, limited depth perception, and lack of force feedback. These limitations place stringent constraints on ophthalmic surgeons and prevent them from performing complex bimanual tasks.

III. Proposed Surgical Setup and System Description

This paper addresses the need to provide surgeons with a stand-alone surgical system that is capable of manipulating or stabilizing the eye while providing bimanual intraocular dexterous operations. The goal of this system is to enable operations in difficult-to-reach areas of the retina. Examples of surgical procedures that benefit from these capabilities include membrane peeling in anterior aspects of the retina, and dual arm and complex manipulation of blood vessels.

Fig. 1 shows the proposed telerobotic slave. Each arm is composed of a 2 Degrees-of-Freedom (DoF) intraorgan dexterity robot (IODR) and a 6-DoF parallel robot. The IODR is introduced because potential applications require additional DoF inside the organ, which is beyond the ability of available 4-DoF minimally invasive surgical tools.

The IODR utilizes a preshaped NiTi tube that bends in 1 DoF as it is extended outside of a straight cannula with a bending radius of 5 mm (see Fig. 7), similar to the work of [32] and [33] on steerable needles. The length of the IODR cannula is chosen as 60 mm based on the length of existing tools. The IODR is connected to the parallel robot via an adjustable lockable universal joint and a connector link, allowing the IODR cannula having two tilting DoFs so that the angle between the cannula and the connection link, as well as the orientation of the connection link with respect to the moving platform is adjustable. With this design, surgeons can initially position and lock the robot at a given "start" configuration, minimizing the required workspace of the parallel robot.

For the parallel robot, we propose the Stewart–Gough platform design [34] due to its rigidity, compactness, positional accuracy, and high payload-to-weight ratio. These advantages were utilized in other robotic systems for medical applications, e.g., [1] and [35]–[39]. The parallel robot is designed to be placed sideways relative to the patient to avoid singularities

associated with large tilting angles of the moving platform (Hunt's singularity [40]).

The dimensions of the parallel robot of each hybrid robotic arm were given in our previous work [11]. These dimensions were chosen to ensure that using both arms allows reaching all points on the retina and to provide orbital manipulation.

IV. Multi-arm Manipulation of Hollow Organs

To fill a hole in the literature addressing constraints that pierce an object, we extend our framework developed in [11] to manipulate and operate on general hollow suspended organs. This general mathematical model applies to all robotic systems with similar constraints.

The instantaneous kinematics of the multiarm robot and the suspended organ is presented in this section. The hollow organ is assumed to be a rigid object movable in 6 DoFs and manipulated by several arms piercing it. Each piercing point presents a 2-DoF constraint specified by maintaining a fixed fulcrum point on the organ. Therefore, for an unconstrained 6-DoF object, three arms (2 DoFs each) are required to fully constrain the system. For a specific hollow organ, upon introducing the anatomic constraints to the general model, we can obtain the corresponding simplified kinematic model. For example, the orbital musculature of the eye can be modeled constraining the eye to only three rotational DoFs; therefore, it only needs two arms to fully constrain the system. Other hollow suspended organs, like the bladder and stomach, can also be modeled after projecting from the 6-D general space to their individual motion space[1].

A. Kinematic Nomenclature

Fig. 8 depicts the organ and the ith hybrid robotic arm. The organ is enlarged for a clearer view of the end-effector (EE) and the organ coordinate frames. The following coordinate systems are defined to assist in the derivation of the system kinematics. The world coordinate system $\{W\}$ is centered at an arbitrarily predetermined point in the patient's forehead with the patient in a supine position. The $\hat{\mathbf{z}}_W$-axis points vertically and $\hat{\mathbf{y}}_W$-axis points superiorly. The Stewart–Gough base coordinate system $\{B_i\}$ of the ith hybrid robot is located at point b_i (the center of the base platform) such that the $\hat{\mathbf{z}}_{B_i}$-axis lies perpendicular to the base of the Stewart–Gough platform, and the $\hat{\mathbf{x}}_{B_i}$-axis lies parallel to $\hat{\mathbf{z}}_W$. The moving platform coordinate system of the ith hybrid robot $\{P_i\}$ lies in the center of the moving platform at point p_i such that the axes lie parallel to $\{B_i\}$ when the Stewart–Gough platform lies in the home configuration. The Stewart–Gough extension arm coordinate system of the ith hybrid robot $\{Q_i\}$ is attached to the distal end of the arm at point q_i, with $\hat{\mathbf{z}}_{Q_i}$ lying along the direction of the insertion needle of the robot $\overrightarrow{q_i n_i}$, and $\hat{\mathbf{x}}_{Q_i}$ fixed during setup procedure. The IODR base coordinate system of the ith hybrid robot $\{N_i\}$ lies at point n_i with the $\hat{\mathbf{z}}_{N_i}$-axis also pointing along the insertion needle length $\overrightarrow{q_i n_i}$ and the $\hat{\mathbf{y}}_{N_i}$-axis rotated from $\hat{\mathbf{y}}_{Q_i}$ by an angle $q_{s_i 1}$ about $\hat{\mathbf{z}}_{N_i}$. The EE coordinate system $\{G_i\}$ lies at point g_i with the $\hat{\mathbf{z}}_{G_i}$-axis pointing in the direction of the EE gripper and the $\hat{\mathbf{y}}_{G_i}$-axis parallel to the $\hat{\mathbf{y}}_{N_i}$-axis. The organ coordinate system $\{O\}$ sits at the rotating center o of the organ with axes parallel to $\{W\}$ when the organ is unactuated by the robot. The additional notations used are defined as the following.

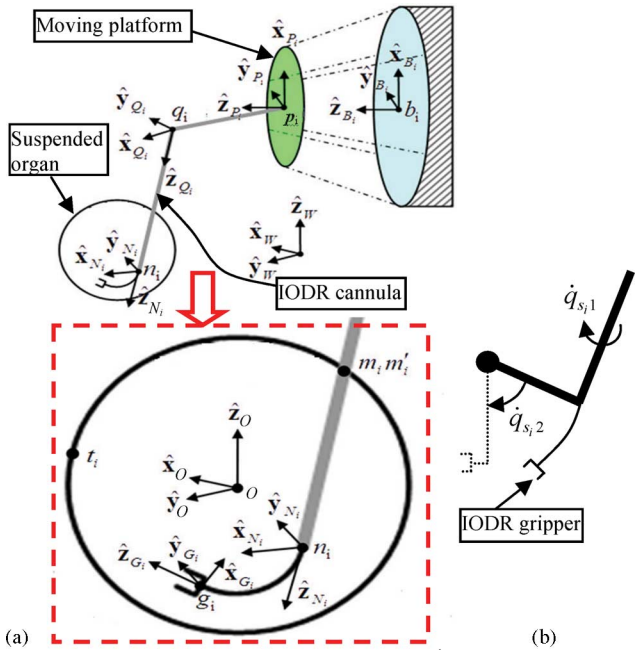

Fig. 8. (a) Kinematic model of the organ and the ith hybrid robot. (b) Kinematic model of the IODR replacing the circular extending cannula with an equivalent rotary joint.

$\{A\}$	a right-handed coordinate frame with $\{\hat{\mathbf{x}}_A, \hat{\mathbf{y}}_A, \hat{\mathbf{z}}_A\}$ as its associated unit vectors and point a as the location of its origin;
${}^A\overrightarrow{ab}$	vector from point a to point b expressed in frame $\{A\}$;
$[\mathbf{b}\times]$	skew-symmetric cross-product matrix [23] of vector $\mathbf{b}$;
i	the index identifying each robotic arm;
$\dot{\mathbf{q}}_{P_i} = [\dot{q}_{P_i 1}, \dot{q}_{P_i 2}, \dot{q}_{P_i 3}, \dot{q}_{P_i 4}, \dot{q}_{P_i 5}, \dot{q}_{P_i 6}]^{\mathrm{T}}$	the active joint speeds of the ith Stewart–Gough platform;
$\dot{\mathbf{q}}_{s_i} = [\dot{q}_{s_i 1}, \dot{q}_{s_i 2}]^{\mathrm{T}}$	joint speeds of the ith IODR. The first component is the rotation speed about the axis of the IODR cannula, and the second component is the bending angular rate of the preshaped tube (Fig. 8(b));
${}^A\mathbf{R}_B$	rotation matrix of frame $\{B\}$ relative to frame $\{A\}$;
$\mathbf{v}^C_{A/B}$,$\boldsymbol{\omega}^C_{A/B}$	relative linear and angular velocities of frame $\{A\}$ relative to $\{B\}$, expressed in $\{C\}$. Unless specifically stated, all vectors in this paper are expressed in $\{W\}$;

[1]The flexibility of these organs is an issue to be addressed individually based on the characteristics of the organ. The issue of organ flexibility is beyond the scope of this paper.

$\mathbf{v}_A$,$\boldsymbol{\omega}_A$	absolute linear and angular velocities of frame $\{A\}$;
$\dot{\mathbf{x}}_A, \dot{\mathbf{x}}_{P_i}, \dot{\mathbf{x}}_o$	twists[2] of frame$\{A\}$ of the ith Stewart–Gough moving platform and of the organ;
$\mathbf{W}(\overrightarrow{a}) = \begin{bmatrix} \mathbf{I}_{3\times3} & [-(\overrightarrow{a})\times] \\ \mathbf{0}_{3\times3} & \mathbf{I}_{3\times3} \end{bmatrix}$	twist transformation operator.

B. System Modeling

The kinematic modeling of the system has to include the kinematic constraints of the incision points on the hollow organ. The following section presents the kinematics of the triple-armed robot with the organ and describes the kinematics of the IODR EE with respect to a target point on the organ.

1) Hybrid Robot: The Jacobian of the Stewart–Gough platform relating the twist of the moving platform $\dot{\mathbf{x}}_{p_i}$ to the joint speeds $\dot{\mathbf{q}}_{p_i}$ is given in (1) [41]. The overall hybrid Jacobian matrix for one robotic arm was obtained as in (2). Appendix A provides derivations of these matrices

$$\mathbf{J}_{P_i}\dot{\mathbf{x}}_{P_i} = \dot{\mathbf{q}}_{P_i} \tag{1}$$

$$\dot{\mathbf{x}}_{G_i} = \mathbf{J}_{h_i}\dot{\mathbf{q}}_{h_i}. \tag{2}$$

2) Organ: Most organs are not free-floating, but rather partially constrained by their surrounding anatomy. A 6-D twist vector is used to describe the motion of the organ

$$\dot{\mathbf{x}}_o = [\dot{\mathbf{x}}_{ol}^{\mathrm{T}}, \dot{\mathbf{x}}_{oa}^{\mathrm{T}}]^{\mathrm{T}} = [\dot{x}, \dot{y}, \dot{z}, \dot{\alpha}, \dot{\beta}, \dot{\gamma}]^{\mathrm{T}} \tag{3}$$

where $x,\ y\ , z\ , \alpha\ , \beta,$ and γ are linear positions and roll–pitch–yaw angles of the organ, and $\dot{\mathbf{x}}_{ol}$ and $\dot{\mathbf{x}}_{oa}$ correspond to the linear and angular velocities of the organ, respectively.

3) Intraorgan Kinematics: The relative linear and angular velocity of the EE with respect to a target point t_i on the inner surface of the organ (Fig. 8) is described as

$$\mathbf{v}_{g_i/t_i} = [\mathbf{I}_{3\times3}, \mathbf{0}_{3\times3}]\mathbf{J}_{h_i}\dot{\mathbf{q}}_{h_i} - \dot{\mathbf{x}}_{ol} - \mathbf{T}_i\dot{\mathbf{x}}_{oa} \tag{4}$$

$$\boldsymbol{\omega}_{g_i/o} = [\mathbf{0}_{3\times3}, \mathbf{I}_{3\times3}]\mathbf{J}_{h_i}\dot{\mathbf{q}}_{h_i} - \dot{\mathbf{x}}_{oa}. \tag{5}$$

Combining (4) and (5) yields the twist of the EE relative to t_i

$$\dot{\mathbf{x}}_{g_i/t_i} = \mathbf{J}_{h_i}\dot{\mathbf{q}}_{h_i} - \mathbf{H}_i\dot{\mathbf{x}}_o \tag{6}$$

where

$$\mathbf{T}_i = [(-\overrightarrow{ot_i})\times] \quad \text{and} \quad \mathbf{H}_i = \begin{bmatrix} \mathbf{I}_{3\times3} & \mathbf{T}_i \\ \mathbf{0}_{3\times3} & \mathbf{I}_{3\times3} \end{bmatrix}.$$

4) Euler Parameterization: The mechanical structure of the hybrid robot in the organ cavity allows only 5 DoFs since independent rotation of the IODR EE about the $\hat{\mathbf{z}}_{G_i}$-axis is unachievable due to the geometry of the organ constraint and the IODR. This rotation is represented by the third Euler angle φ_i in a w–v–w sequence [41]. For the purposes of path planning and control, the twist of the EE can be parameterized using w–v–w Euler angles while eliminating the third Euler angle by using a degenerate matrix $\mathbf{K}_i$, (7). $\mathbf{K}_i$ is defined in Appendix B. Inserting this new parameterization in (6) yields a relation between the achievable independent velocities and the joint parameters of the hybrid system as in (8) below:

$$\tilde{\dot{\mathbf{x}}}_{g_i/t_i} = \mathbf{K}_i\dot{\mathbf{x}}_{g_i/t_i} \tag{7}$$

$$\tilde{\dot{\mathbf{x}}}_{g_i/t_i} + \mathbf{K}_i\mathbf{H}_i\dot{\mathbf{x}}_o = \mathbf{K}_i\mathbf{J}_{h_i}\dot{\mathbf{q}}_{h_i}. \tag{8}$$

5) Overall Organ–Robot System: The robotic system must be constrained such that the multitude n_a of hybrid robotic arms moves synchronously to control the organ without tearing the insertion points. Let m_i designate the ith incision point on the organ, $i = 1, 2, 3, \ldots, n_a$. Let m_i' designate the corresponding point on the IODR cannula of the ith robotic arm that is instantaneously coincident with m_i. To prevent damage to the anatomy, an equality constraint must be imposed between the projections of the linear velocities of m_i and m_i' on a plane perpendicular to the longitudinal axis of the ith IODR cannula. These conditions are derived in Appendix C and given as

$$\hat{\mathbf{x}}_{Q_i}^{\mathrm{T}}\mathbf{F}_i\dot{\mathbf{q}}_{h_i} = \hat{\mathbf{x}}_{Q_i}^{\mathrm{T}}(\dot{\mathbf{x}}_{ol} + \mathbf{M}_i\dot{\mathbf{x}}_{oa}), \quad i = 1,\ 2,\ 3, \ldots, n_a \tag{9}$$

$$\hat{\mathbf{y}}_{Q_i}^{\mathrm{T}}\mathbf{F}_i\dot{\mathbf{q}}_{h_i} = \hat{\mathbf{y}}_{Q_i}^{\mathrm{T}}(\dot{\mathbf{x}}_{ol} + \mathbf{M}_i\dot{\mathbf{x}}_{oa}), \quad i = 1,\ 2,\ 3, \ldots, n_a. \tag{10}$$

Equations (9) and (10) constitute $2n_a$ scalar equations that provide the conditions for the organ to be constrained by n_a robotic arms inserted into it. For the organ to be fully constrained by the robotic arms, (9) and (10) should have a rank equal to the dimension of the organ twist $\dot{\mathbf{x}}_o$. If the organ is free-floating, then the rank should be six, and therefore, a minimum of three robotic arms is necessary to effectively stabilize the organ. If the organ is constrained from translation (e.g., the eye), the required rank is three, and hence, the minimal number of arms is two. This justifies the design of the dual-arm ophthalmic surgical system depicted in Fig. 1.

Combining (9) and (10) with the twist of the hybrid robotic arms $\tilde{\dot{\mathbf{x}}}_{g_i/t_i}$ for $i = 1,\ 2$, and 3 yields the kinematics of the overall system composed of the organ and the three robotic arms; see (11) below. Definitions of matrices $\mathbf{G}_i$ and $\mathbf{P}_i$ are given in Appendix C:

$$\underbrace{\begin{bmatrix} \mathbf{K}_1\mathbf{J}_{h_1} & \mathbf{0}_{5\times8} & \mathbf{0}_{5\times8} \\ \mathbf{0}_{5\times8} & \mathbf{K}_2\mathbf{J}_{h_2} & \mathbf{0}_{5\times8} \\ \mathbf{0}_{5\times8} & \mathbf{0}_{5\times8} & \mathbf{K}_3\mathbf{J}_{h_3} \\ \mathbf{G}_1\mathbf{F}_1 & \mathbf{0}_{2\times8} & \mathbf{0}_{2\times8} \\ \mathbf{0}_{2\times8} & \mathbf{G}_2\mathbf{F}_2 & \mathbf{0}_{2\times8} \\ \mathbf{0}_{2\times8} & \mathbf{0}_{2\times8} & \mathbf{G}_3\mathbf{F}_3 \end{bmatrix}}_{\mathbf{J}_I} \begin{bmatrix} \dot{\mathbf{q}}_{h_1} \\ \dot{\mathbf{q}}_{h_2} \\ \dot{\mathbf{q}}_{h_3} \end{bmatrix}$$

$$= \underbrace{\begin{bmatrix} \mathbf{I}_{5\times5} & \mathbf{0}_{5\times5} & \mathbf{0}_{5\times5} & \mathbf{K}_1\mathbf{H}_1 \\ \mathbf{0}_{5\times5} & \mathbf{I}_{5\times5} & \mathbf{0}_{5\times5} & \mathbf{K}_2\mathbf{H}_2 \\ \mathbf{0}_{5\times5} & \mathbf{0}_{5\times5} & \mathbf{I}_{5\times5} & \mathbf{K}_3\mathbf{H}_3 \\ \mathbf{0}_{2\times5} & \mathbf{0}_{2\times5} & \mathbf{0}_{2\times5} & \mathbf{G}_1\mathbf{P}_1 \\ \mathbf{0}_{2\times5} & \mathbf{0}_{2\times5} & \mathbf{0}_{2\times5} & \mathbf{G}_2\mathbf{P}_2 \\ \mathbf{0}_{2\times5} & \mathbf{0}_{2\times5} & \mathbf{0}_{2\times5} & \mathbf{G}_3\mathbf{P}_3 \end{bmatrix}}_{\mathbf{J}_O} \begin{bmatrix} \tilde{\dot{\mathbf{x}}}_{g_1/t_1} \\ \tilde{\dot{\mathbf{x}}}_{g_2/t_2} \\ \tilde{\dot{\mathbf{x}}}_{g_3/t_3} \\ \dot{\mathbf{x}}_o \end{bmatrix}. \tag{11}$$

[2]throughout this paper, a twist is defined as a 6-D column vector with linear velocity preceding the angular velocity.

In Wen's work [15], the kinematic and static model of a two-finger grasping manipulator was given. By modeling the contact between fingers and the payload mathematically, the authors derived the differential kinematic relationship. Our application differs because the insertion constraint produces a constantly changing contact point on the robot arm. Equation (11) is applicable to general robotic systems with insertion constraints piercing into hollow objects.

C. Jacobian Normalization

Robot kinetostatic performance can be evaluated by examining the characteristics of the robot Jacobian. Several commonly used performance measures, like the condition number [23], the manipulability index [19], and kinematic conditioning [42], are based on the robot Jacobian. However, directly using the Jacobian for performance evaluation leads to meaningless results due to the inhomogeneity of physical units of its components [43]. Normalization of the Jacobian is necessary in order to ensure meaningful results when calculating the singular values. Inhomogeneity of the units of the Jacobian stems from the inhomogeneity of the units in the twist or joint space; hence, different approaches to normalize the Jacobian matrix have been used. Stocco *et al*. [44] used scaling matrices corresponding to ranges of joint and task-space variables to pre- and post-multiply the Jacobian for normalization. Angeles [23] proposed to use the characteristic length to normalize the portion of the Jacobian bearing the unit of length and use kinematic conditioning index (KCI), which is defined as the ratio of the smallest and largest singular value of a normalized Jacobian, for performance evaluation. Gosselin and Angeles [26] found a Jacobian scaling matrix by using a physically meaningful transformation of the EE twist that homogenizes the units of the transformed twist.

Regardless of the method used, the designer has to make an intelligent decision about the scaling/normalization factors of the Jacobian prior to the calculation of the condition index [44]. The methodology used in this paper relies on the use of individual characteristic lengths for the serial and the parallel portions of each robotic arm in Fig. 1.

Equations (12)–(14) specify the units of the individual vectors and submatrices of (14). The brackets are used to designate units of a vector or a matrix, where [m] and [s] denote meters and seconds, respectively

$$\begin{aligned}
\left[\tilde{\dot{\mathbf{x}}}_{g_i/t_i}\right] &= \left[\,[\mathrm{m/s}]_{1\times 3} \quad [1/\mathrm{s}]_{1\times 2}\,\right]^{\mathrm{T}} \\
[\dot{\mathbf{x}}_o] &= \left[\,[\mathrm{m/s}]_{1\times 3} \quad [1/\mathrm{s}]_{1\times 3}\,\right]^{\mathrm{T}} \\
[\dot{\mathbf{q}}_{h_i}] &= \left[\,[\mathrm{m/s}]_{1\times 6} \quad [1/\mathrm{s}]_{1\times 2}\,\right]^{\mathrm{T}} \qquad (12) \\
[\mathbf{G}_i\mathbf{P}_i] &= \left[\,[1]_{2\times 3} \quad [\mathrm{m}]_{2\times 3}\,\right] \\
[\mathbf{G}_i\mathbf{F}_i] &= \left[\,[1]_{2\times 6} \quad [0]_{2\times 2}\,\right] \qquad (13) \\
[\mathbf{K}_i\mathbf{H}_i] &= \begin{bmatrix} [1]_{3\times 3} & [\mathrm{m}]_{3\times 3} \\ [0]_{2\times 3} & [1]_{2\times 3} \end{bmatrix} \\
[\mathbf{K}_i\mathbf{J}_{h_i}] &= \begin{bmatrix} [1]_{3\times 6} & [\mathrm{m}]_{3\times 2} \\ [1/\mathrm{m}]_{2\times 6} & [1]_{2\times 2} \end{bmatrix}. \qquad (14)
\end{aligned}$$

The Jacobians $\mathbf{J}_I$ and $\mathbf{J}_O$ do not possess uniform units, and using a single characteristic length to normalize both of them is not possible because the robotic arms of Fig. 1 include both serial and parallel portions. Therefore, in order to evaluate the performance of the robotic system for different applications as a whole, we simultaneously normalize $\mathbf{J}_I$ and $\mathbf{J}_O$. This can be achieved by inspecting the units and the physical meaning of all submatrices in (14) while relating each matrix block to the kinematics of the parallel robot, the IODR, or the organ.

The Jacobian matrix $\mathbf{J}_O$ characterizes the velocities of the rotating organ and the desired EE. $\mathbf{J}_O$ is homogenized using the radius of the organ at the target point as the characteristic length. It is this radius, as measured with respect to the instantaneous center of rotation, that imparts a linear velocity to point t_i as a result of the angular velocity of the organ. The top right nine components of $\mathbf{K}_i\mathbf{H}_i, i = 1, 2,$ and 3 of (11), bear the unit of [m]. Hence, we divide them by the radius of the organ at the target point, L_r in order to normalize them. This approach is congruent with [14] and [44], which used scaling matrices relating the units of twist of the EE. The same treatment is also carried out to the rightmost six components of each matrix block $\mathbf{G}_i\mathbf{P}_i$, where we divide them by L_r as well.

Jacobian $\mathbf{J}_I$ describes the geometry of both the parallel robot and the IODR. Therefore, we use both L_p, the length of the connection link of the parallel robot ($\overrightarrow{p_iq_i}$ in Fig. 8), and L_s, the bending radius of the inner tube of the IODR as characteristic lengths. We multiply L_p to those components in $\mathbf{K}_i\mathbf{J}_{h_i}$ that bear the unit of [1/m]. We also divide the components that bear the unit of [m] by L_s. This results in a normalized input Jacobian $\mathbf{J}_I$ that is dimensionless. While previous works suggested using the radius of the moving platform for normalization [23], [27], we chose L_p because we are interested in the angular and linear velocities at point q_i (Fig. 8). L_p is the scaling factor of the linear velocity at point q_i stemming from a unit angular velocity of the moving platform. Similarly, the circular bending tube of the IODR is modeled as a virtual rotary joint (Fig. 8); hence, the bending radius L_s is used to normalize the components related to the IODR.

V. Motivating Case Study: Ophthalmic Microsurgery

A. Model of the System in Ophthalmic Surgery

The eye is constrained by its surrounding musculature to have only three rotational DoFs about its center. The twist of the organ in (3) is reduced to a 3-D vector as in (15), shown below. The linear and angular velocities of the robot arm EE relative to a target point t_i on the retina are given by (16) and (17), shown below:

$$\dot{\mathbf{x}}_e = [\dot{\alpha}, \dot{\beta}, \dot{\gamma}]^{\mathrm{T}} \qquad (15)$$

$$\mathbf{v}_{g_i/t_i} = [\mathbf{I}_{3\times 3}, \mathbf{0}_{3\times 3}]\mathbf{J}_{h_i}\dot{\mathbf{q}}_{h_i} - \mathbf{T}_i\dot{\mathbf{x}}_e \qquad (16)$$

$$\boldsymbol{\omega}_{g_i/e} = [\mathbf{0}_{3\times 3}, \mathbf{I}_{3\times 3}]\mathbf{J}_{h_i}\dot{\mathbf{q}}_{h_i} - \dot{\mathbf{x}}_e. \qquad (17)$$

Combining (16) and (17) yields the relative twist of the EE of each arm with respect to the target point on the retina (18), where $\mathbf{D}_i = [\mathbf{T}_i^{\mathrm{T}}, \mathbf{I}_{3\times 3}]^{\mathrm{T}}$. The 5-D constrained twist of the IODR EE in

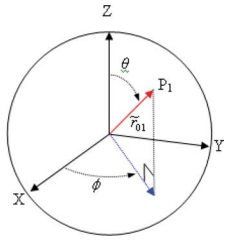

Fig. 9. Definition of a point on the retina based on Euler angles.

(8) simplifies to (19), shown below. The overall system Jacobian is given by (20), shown below:

$$\dot{\mathbf{x}}_{g_i/t_i} = \mathbf{J}_{h_i}\dot{\mathbf{q}}_{h_i} - \mathbf{D}_i\dot{\mathbf{x}}_e \tag{18}$$

$$\tilde{\dot{\mathbf{x}}}_{g_i/t_i} + \mathbf{K}_i\mathbf{D}_i\dot{\mathbf{x}}_e = \mathbf{K}_i\mathbf{J}_{h_i}\dot{\mathbf{q}}_{h_i} \tag{19}$$

$$\underbrace{\begin{bmatrix} \mathbf{K}_1\mathbf{J}_{h_1} & \mathbf{0}_{5\times 8} \\ \mathbf{0}_{5\times 8} & \mathbf{K}_2\mathbf{J}_{h_2} \\ \mathbf{G}_1\mathbf{F}_1 & \mathbf{0}_{2\times 8} \\ \mathbf{0}_{2\times 8} & \mathbf{G}_2\mathbf{F}_2 \end{bmatrix}}_{\mathbf{M}} \begin{bmatrix} \dot{\mathbf{q}}_{h_1} \\ \dot{\mathbf{q}}_{h_2} \end{bmatrix} = \underbrace{\begin{bmatrix} \mathbf{I}_{5\times 5} & \mathbf{0}_{5\times 5} & \mathbf{K}_1\mathbf{D}_1 \\ \mathbf{0}_{5\times 5} & \mathbf{I}_{5\times 5} & \mathbf{K}_2\mathbf{D}_2 \\ \underbrace{\mathbf{0}_{2\times 5}}_{\mathbf{N}_1} & \underbrace{\mathbf{0}_{2\times 5}}_{\mathbf{N}_1} & \underbrace{\mathbf{G}_1\mathbf{M}_1}_{\mathbf{N}_2} \\ \mathbf{0}_{2\times 5} & \mathbf{0}_{2\times 5} & \mathbf{G}_2\mathbf{M}_2 \end{bmatrix}}_{\mathbf{N}} \times \begin{bmatrix} \tilde{\dot{\mathbf{x}}}_{g_1/t_1} \\ \tilde{\dot{\mathbf{x}}}_{g_2/t_2} \\ \dot{\mathbf{x}}_e \end{bmatrix}. \tag{20}$$

Rewriting (20) using matrices $\mathbf{M}$ and $\mathbf{N}$, we obtain (21), shown below, where $\dot{\mathbf{q}}_h = [\dot{\mathbf{q}}_{h_1}^{\mathrm{T}}, \dot{\mathbf{q}}_{h_2}^{\mathrm{T}}]^{\mathrm{T}}$, and $\tilde{\dot{\mathbf{x}}}_{g/t} = [\tilde{\dot{\mathbf{x}}}_{g_1/t_1}^{\mathrm{T}}, \tilde{\dot{\mathbf{x}}}_{g_2/t_2}^{\mathrm{T}}]^{\mathrm{T}}$. Note that intraocular manipulation can be modeled by setting $\dot{\mathbf{x}}_e = \mathbf{0}$. Similarly, organ manipulation can be represented by setting $\tilde{\dot{\mathbf{x}}}_{g/t} = \mathbf{0}$

$$\mathbf{M}\dot{\mathbf{q}}_h = \mathbf{N}_1\tilde{\dot{\mathbf{x}}}_{g/t} + \mathbf{N}_2\dot{\mathbf{x}}_e. \tag{21}$$

B. Dexterity Evaluation for All Four Manipulation Cases

Fig. 4 showed four manipulation cases. The corresponding dexterity measures for these cases are derived in this section. Throughout this section, two incision points are specified by angles $[\theta,\ \phi]^{\mathrm{T}} = [\pi/3, \pi/3]^{\mathrm{T}}$ and $[\pi/3, \pi]^{\mathrm{T}}$, as defined in Fig. 9.

1) Case 1: Intraocular Dexterity: The aim of intraocular dexterity evaluation is to compare the performance of the system with or without the IODR. The setup without the IODR (7-DoF setup) represents the current ophthalmic surgical setup based on rigid tools. For the setup without an IODR, a straight cannula capable of rotating about its own longitudinal axis was modeled, yielding a 7-DoF robotic arm. The Jacobian matrix for the 7-DoF robotic arm is

$$\mathbf{J}_{7_i} = \begin{bmatrix} \mathbf{B}_i\mathbf{A}_i\mathbf{J}_{P_i}^{-1}, & \mathbf{0}_{3\times 1} \\ & \hat{\mathbf{z}}_{Q_i} \end{bmatrix}$$

as in (22) and (23), shown below. In the second configuration (8-DoF setup), the robotic arms are equipped with the IODR of Figs. 7 and 8(b). This setup represents the robotic system of Fig. 1 with intraocular dexterity.

In Section IV-C, multiple characteristic lengths were used to normalize the system Jacobian. For manipulation case 1, the translational and rotational dexterities were quantified by investigating the upper and lower three rows of $\mathbf{J}_{7_i}$ and $\mathbf{J}_{h_i}$. In this paper, translational and rotational dexterities are individually investigated in order to provide insight of the robot to perform specific procedures requiring translations or rotations. Equations (22) and (24), shown below, give the normalized sub-Jacobians for translational motions of 7-DoF and 8-DoF setup, while (23) and (25), shown below, give the normalized sub-Jacobians for rotational motions of both setups:

$$\mathbf{J}_{7\mathrm{DoF}\_t} = [\mathbf{I}_{3\times 3}, \mathbf{0}_{3\times 3}] \begin{bmatrix} \mathbf{B}_i\mathbf{A}_i\mathbf{J}_{P_i}^{-1}, & \mathbf{0}_{3\times 1} \\ & \hat{\mathbf{z}}_{Q_i} \end{bmatrix} \begin{bmatrix} \mathbf{I}_{6\times 6} & \mathbf{0}_{6\times 1} \\ \mathbf{0}_{1\times 6} & 1/L_s \end{bmatrix} \tag{22}$$

$$\mathbf{J}_{7\mathrm{DoF}\_r} = [\mathbf{0}_{3\times 3}, \mathbf{I}_{3\times 3}] \begin{bmatrix} \mathbf{B}_i\mathbf{A}_i\mathbf{J}_{P_i}^{-1}, & \mathbf{0}_{3\times 1} \\ & \hat{\mathbf{z}}_{Q_i} \end{bmatrix} \begin{bmatrix} L_P\mathbf{I}_{6\times 6} & \mathbf{0}_{6\times 1} \\ \mathbf{0}_{1\times 6} & 1 \end{bmatrix} \tag{23}$$

$$\mathbf{J}_{8\mathrm{DoF}\_t} = [\mathbf{I}_{3\times 3}, \mathbf{0}_{3\times 3}]\mathbf{J}_{h_i} \begin{bmatrix} \mathbf{I}_{6\times 6} & \mathbf{0}_{6\times 2} \\ \mathbf{0}_{2\times 6} & \mathbf{I}_{2\times 2}/L_s \end{bmatrix} \tag{24}$$

$$\mathbf{J}_{8\mathrm{DoF}\_r} = [\mathbf{0}_{3\times 3}, \mathbf{I}_{3\times 3}]\mathbf{J}_{h_i} \begin{bmatrix} L_P\mathbf{I}_{6\times 6} & \mathbf{0}_{6\times 2} \\ \mathbf{0}_{2\times 6} & \mathbf{I}_{2\times 2} \end{bmatrix}. \tag{25}$$

Based on clinical observation of vitrectomy procedures, we estimate that most procedures are performed on an area of $\pm 20^\circ$ around a chosen center point on the retina. The lower hemisphere of the retina is divided into a number of $\pm 20^\circ$ patches. These patches represent different possible surgical sites. The local KCI (LKCI) for each patch is calculated by averaging the KCI values over the scanned area and plotting the results throughout the workspace. In these plots, θ and ϕ are the first two w–v–w Euler angles that locate the center point of each patch (see Fig. 9).

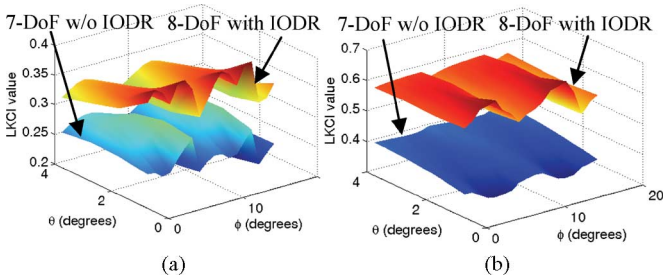

Fig. 10. LKCI for intraocular dexterity. (a) Translation. (b) Rotational.

TABLE I
AVERAGE INTRAOCULAR GKCI OVER THE WHOLE WORKSPACE

	Rotary Cannula (no IODR)	With IODR	Improvement
Translational GKCI	0.2549	0.3355	31.62%
Rotational GKCI	0.3660	0.5773	57.73%

Fig. 10 shows that the translational and rotational dexterities are significantly improved throughout the workspace by the use of the IODR. Table I also presents the global KCI (GKCI) defined as the average of LKCI values over all workspace patches.

Fig. 11 shows the robot's intraocular tangential dexterity on a specified surgical site: $120^\circ < \theta < 160^\circ$and $20^\circ < \phi < 100^\circ$. The manipulability ellipsoids of the robot while reaching each

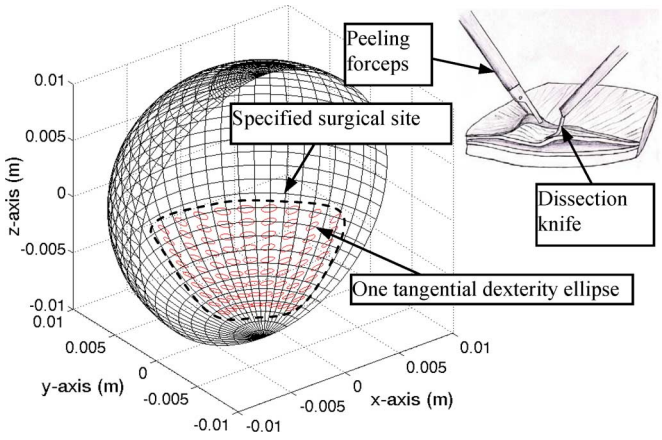

Fig. 11. Example of bimanual membrane peeling procedure (only half of the eyeball is shown). The surgical site represents the membrane. Each ellipse represents the intersection of a manipulability ellipsoid with its local tangent plane of the eye.

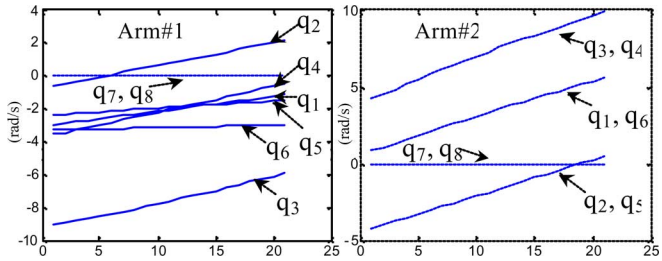

Fig. 12. Case 2. Joint rates for orbital manipulation with constraints. The x-axis describes the rotation sequence and the y-axis describes the joint rates. In both plots, solid lines represent the joint rates for the parallel robot in millimeters per second, and dotted lines represent the joint rates for the IODR in radians per second.

site point have been intersected with the local tangent plane of the eye. The resulting ellipses represent the robot's dexterity in performing tangential motions, such as tissue dissection. This information can be used for planning specific surgical tasks, e.g., bimanual membrane peeling.

2) Case 2: Orbital Dexterity With Constraints: This case is represented by Fig. 4(b). In this case, the two arms are constrained to maintain zero relative motion with respect to a target point on the retina while manipulating the eyeball. The target point was selected to be $[5\pi/6, 0]^{\mathrm{T}}$, defined in the eye-attached coordinate system $\{E\}$. Frame $\{E\}$ is defined similarly as the organ coordinate system $\{O\}$ in Fig. 8, and represents the rotation of the eye relative to $\{W\}$.

To verify the accuracy of our derivation, we specified a desired rotation velocity of the eye as 10° per second about $\hat{\mathbf{y}}_{\mathbf{w}}$-axis in Fig. 8, and calculated the joint velocities through the inverse of the Jacobian. For the task of rotating the eye by fixing the EE to the target point, the two IODRs and the eyeball form a rigid body allowing no relative motion in-between. Therefore, the rates of the IODR joints are expected to be zeros. Fig. 12 confirms the correctness of our derivation.

The robot dexterity in tilting the eye 20° in all directions from its unperturbed "home" configuration was evaluated. The LKCI values are shown in Fig. 13 as small circle points, where each

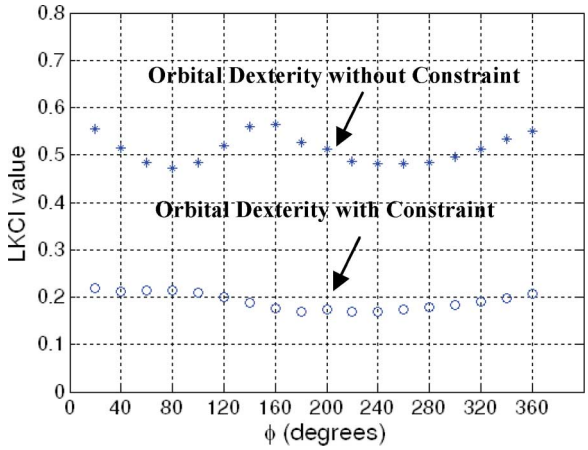

Fig. 13. LKCIs of orbital manipulation with and without constraints.

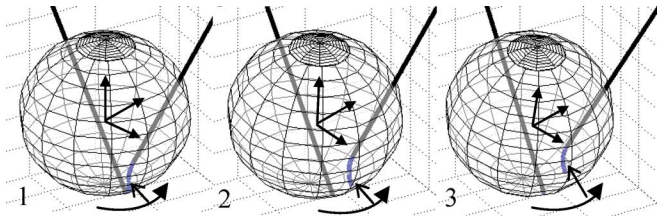

Fig. 14. Simultaneous orbital and intraocular manipulation. The eyeball is rotated while one arm scans the surface of the retina.

point denotes the LKCI value of the system when rotating the eye along the specified path.

3) Case 3: Orbital Dexterity Without Constraints: Since $\tilde{\dot{\mathbf{x}}}_{g/t}$ is not constrained, (19) is substituted into (21), yielding the system Jacobian for this case:

$$(\mathbf{M} - \mathbf{N}_1\mathbf{O}_1)\dot{\mathbf{q}}_h = (\mathbf{N}_1\mathbf{O}_2 + \mathbf{N}_2)\dot{\mathbf{x}}_e \tag{26}$$

where

$$\mathbf{O}_1 = \begin{bmatrix} \mathbf{K}_1\mathbf{J}_{h_1} & \mathbf{0}_{5\times 8} \\ \mathbf{0}_{5\times 8} & \mathbf{K}_2\mathbf{J}_{h_2} \end{bmatrix} \quad \text{and} \quad \mathbf{O}_2 = \begin{bmatrix} -\mathbf{K}_1\mathbf{D}_1 \\ -\mathbf{K}_2\mathbf{D}_2 \end{bmatrix}.$$

The robot dexterity in tilting the eye 20° in all directions from its "home" configuration was evaluated. The LKCI based on (26) was plotted in Fig. 13 using star symbols. Removing the constraints of zero relative velocity of the EE increases the orbital manipulation dexterity of the system.

4) Case 4: Simultaneous Orbital and Intraocular Dexterity: In case 4, both arms coordinate to manipulate the eyeball. One arm also operates inside the eye along a specified path. The overall dexterity of the robot in executing this combined motion is evaluated. The eye is rotated about $\hat{\mathbf{y}}_{\mathbf{w}}$-axis in Fig. 8, while one robotic arm scans the retina independently. An illustration of this combined motion is depicted in Fig. 14.

Fig. 15 shows the translational and rotational KCI values separately. Since we have put more constraints on the system (both orbital manipulation constraint and intraocular scanning constraint), the KCI values are smaller than for cases 1–3. In current practice, ophthalmic surgeons are not capable of performing simultaneous manipulations, as defined in case 4. We plan on using the robot to decrease the operation time and the number of delicate regrasping operations.

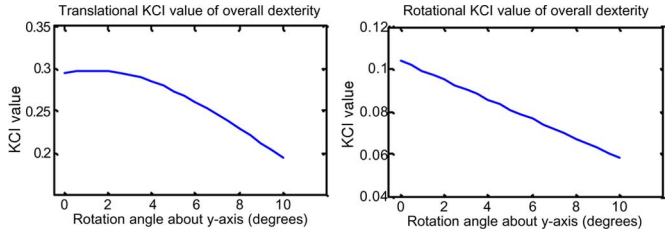

Fig. 15. Translational and rotational KCI values of the robotic system for tracing a specified path as well as performing orbital manipulation.

VI. Conclusion

This paper has presented a new hybrid robotic system being developed for surgical procedures associated with hollow suspended organs. Four simulation cases were proposed to define manipulation procedures for hollow organ surgeries. Specifically, the presented cases were examined in ophthalmic surgery where the eyeball is a partially constrained hollow suspended organ. Dexterity improvements in manipulation and operation of the eyeball were quantified while using the proposed robot compared to traditional tools. Moreover, a mathematical framework of a multiarmed hybrid robotic system with insertion constraints was established. This model is added to the extensively investigated model of multibody robots/multifinger hands and is applicable to any robotic system with insertion constraints. In addition, the approach of using multiple characteristic lengths to evaluate the kinematic performance of highly hybrid robotic system was proposed. Our future research includes experimental validation of the robotic system shown in Fig. 1, which is currently under construction.

Appendix A

As shown in Fig. 8(a), in order to transform the linear and angular velocities from Stewart–Gough platform center to frame$\{Q_i\}$, we have

$$\mathbf{v}_{Q_i} = \mathbf{v}_{P_i} + \boldsymbol{\omega}_{P_i} \times (\overrightarrow{p_i q_i}) \tag{27}$$

$$\boldsymbol{\omega}_{Q_i} = \boldsymbol{\omega}_{P_i}. \tag{28}$$

Writing (27) and (28) in matrix form results in the twist of the distal end q_i of the connection link

$$\dot{\mathbf{x}}_{Q_i} = \mathbf{A}_i \dot{\mathbf{x}}_{P_i} \tag{29}$$

where $\mathbf{A}_i = \mathbf{W}(\overrightarrow{p_i q_i})$ is the twist transformation matrix defined in Section IV-A.

Similarly, we have $\mathbf{B}_i = \mathbf{W}(\overrightarrow{q_i n_i})$ and $\mathbf{C}_i = \mathbf{W}(\overrightarrow{n_i g_i})$ to calculate the twist of point g_i contributed by the Stewart–Gough platform. By incorporating the two serial DoFs of the IODR, we obtain the twist of point g_i as

$$\dot{\mathbf{x}}_{G_i} = \mathbf{C}_i \mathbf{B}_i \dot{\mathbf{x}}_{Q_i} + \mathbf{C}_i \begin{bmatrix} \mathbf{0} \\ \hat{\mathbf{z}}_{Q_i} \end{bmatrix} \dot{q}_{s_i 1} + \begin{bmatrix} \mathrm{r}\hat{\mathbf{z}}_{G_i} \\ \hat{\mathbf{y}}_{N_i} \end{bmatrix} \dot{q}_{s_i 2}. \tag{30}$$

Thus, we get the Jacobian $\mathbf{J}_{s_i}$ of the IODR as

$$\dot{\mathbf{x}}_{G_i} = \mathbf{C}_i \mathbf{B}_i \dot{\mathbf{x}}_{Q_i} + \mathbf{J}_{s_i} \dot{\mathbf{q}}_{s_i} \tag{31}$$

where

$$\mathbf{J}_{s_i} = \begin{bmatrix} [(-\overrightarrow{n_i g_i}) \times] \hat{\mathbf{z}}_{Q_i} & \mathrm{r}\hat{\mathbf{z}}_{G_i} \\ \hat{\mathbf{z}}_{Q_i} & \hat{\mathbf{y}}_{N_i} \end{bmatrix}$$

including the speeds of rotation about the axis of the IODR cannula and the bending of the precurved NiTi tube. The hybrid Jacobian matrix relating the twist of point g_i and all eight inputs of one arm was obtained as in (2), where $\mathbf{J}_{h_i} = \left[\mathbf{C}_i \mathbf{B}_i \mathbf{A}_i \mathbf{J}_{P_i}^{-1}, \mathbf{J}_{s_i}\right]$, and $\dot{\mathbf{q}}_{h_i} = \left[\dot{\mathbf{q}}_{p_i}^{\mathrm{T}}, \dot{\mathbf{q}}_{s_i}^{\mathrm{T}}\right]^{\mathrm{T}}$.

Appendix B

The 5×1 Euler angle parameterization of the desired ith EE velocity $\tilde{\dot{\mathbf{x}}}_{g_i/t_i}$ is related in the text to the general twist of the ith robot EE,$\dot{\mathbf{x}}_{g_i/t_i}$ by the degenerate matrix $\mathbf{K}_i$. The matrix is derived using the relationship found in the literature [45] relating the Cartesian angular velocities to the Euler angle velocities

$$[\omega_x, \omega_y, \omega_z]^{\mathrm{T}} = \mathbf{R}_i [\dot{\phi}, \dot{\theta}, \dot{\phi}]^{\mathrm{T}} \tag{32}$$

where

$$\mathbf{R}_i = \begin{bmatrix} 0 & -\sin(\phi_i) & \cos(\phi_i)\sin(\theta_i) \\ 0 & \cos(\phi_i) & \sin(\phi_i)\sin(\theta_i) \\ 1 & 0 & \cos(\theta_i) \end{bmatrix}.$$

With the aforementioned relationship, the general twist of a system $\dot{\mathbf{x}}$ can be related to the 6×1 Euler angle twist $[\dot{x}, \dot{y}, \dot{z}, \dot{\phi}, \dot{\theta}, \dot{\phi}]^{\mathrm{T}}$ as follows:

$$[\dot{x}, \dot{y}, \dot{z}, \dot{\phi}, \dot{\theta}, \dot{\phi}]^{\mathrm{T}} = \mathbf{S}_i \dot{\mathbf{x}} \tag{33}$$

where

$$\mathbf{S}_i = \begin{bmatrix} \mathbf{I} & \mathbf{0} \\ \mathbf{0} & \mathbf{R}_i^{-1} \end{bmatrix}.$$

The 5×1 Euler parameterization used in the path planning equation of the text is derived by applying a 5×6 degenerate matrix to the 6×1 Euler angle twist as follows:

$$\tilde{\dot{\mathbf{x}}} = [\mathbf{I}_{5\times5}, \mathbf{0}_{5\times1}][\dot{x}, \dot{y}, \dot{z}, \dot{\phi}, \dot{\theta}, \dot{\phi}]^{\mathrm{T}}. \tag{34}$$

Substituting the relationship between the generalized and the 6×1 Euler angle twist (33) yields the matrix $\mathbf{K}_i$ as follows:

$$\tilde{\dot{\mathbf{x}}} = \mathbf{K}_i \dot{\mathbf{x}} \qquad \text{where} \qquad \mathbf{K}_i = [\mathbf{I}_{5\times5}, \mathbf{0}_{5\times1}]\mathbf{S}_i. \tag{35}$$

Appendix C

In the text, we specified the constraint that each insertion arm moves at the insertion point only with the velocity equal to the velocity of the organ surface at that point, plus any velocity along the insertion needle. To assist in the development of this constraint, point m_i is defined at the insertion point on the surface of the organ and m_i' is defined as the point on the insertion needle instantaneously coincident with m_i (Fig. 8). The velocity of m_i' must be equal to the velocity of point m_i in the plane perpendicular to the needle axis

$$\mathbf{v}_{m_i' \perp} = \mathbf{v}_{m_i \perp}. \tag{36}$$

Taking a dot product in the directions $\hat{\mathbf{x}}_{Q_i}$ and $\hat{\mathbf{y}}_{Q_i}$ yields two independent constraint equations

$$\hat{\mathbf{x}}_{Q_i}^{\mathrm{T}}\,\mathbf{v}_{m_i'} = \hat{\mathbf{x}}_{Q_i}^{\mathrm{T}}\,\mathbf{v}_{m_i} \tag{37}$$

$$\hat{\mathbf{y}}_{Q_i}^{\mathrm{T}}\,\mathbf{v}_{m_i'} = \hat{\mathbf{y}}_{Q_i}^{\mathrm{T}}\,\mathbf{v}_{m_i}. \tag{38}$$

These constraints can be expressed in terms of the joint angles and organ velocity by relating the velocities of point m_i and m_i' to the robot and organ coordinate systems. The velocity of point m_i' can be related to the velocity of frame $\{Q_i\}$ as

$$\mathbf{v}_{m_i'} = \mathbf{v}_{Q_i} + \boldsymbol{\omega}_{Q_i} \times \overrightarrow{q_i m}_i \tag{39}$$

By substituting the twist of frame$\{Q_i\}$,(39) becomes

$$\mathbf{v}_{m_i'} = [\mathbf{I}_{3\times 3}, \mathbf{0}_{3\times 3}]\dot{\mathbf{x}}_{Q_i} + \mathbf{E}_i[\mathbf{0}_{3\times 3}, \mathbf{I}_{3\times 3}]\dot{\mathbf{x}}_{Q_i} \tag{40}$$

where

$$\mathbf{E}_i = [(-\overrightarrow{q_i m_i})\times].$$

Inserting (29) and (1) and writing in terms of the hybrid joint parameters $\dot{\mathbf{q}}_{h_i}$ yields

$$\mathbf{v}_{m_i'} = \mathbf{F}_i\dot{\mathbf{q}}_{h_i} \tag{41}$$

where

$$\mathbf{F}_i = \left([\mathbf{I}_{3\times 3}, \mathbf{0}_{3\times 3}] + \mathbf{E}_i[\mathbf{0}_{3\times 3}, \mathbf{I}_{3\times 3}]\right)\mathbf{A}_i\mathbf{J}_{P_i}^{-1}[\mathbf{I}_{6\times 6}, \mathbf{0}_{6\times 2}].$$

An expression for the velocity of the insertion point m_i can be related to the desired organ velocity, yielding

$$\mathbf{v}_{m_i} = \dot{\mathbf{x}}_{ol} + \mathbf{M}_i\dot{\mathbf{x}}_{oa} \tag{42}$$

where

$$\mathbf{M}_i = [(-\overrightarrow{om_i})\times].$$

Substituting (41) and (42) into (37) and (38) yields the final constraint equations given the rigid-body motion of the organ–robot system

$$\hat{\mathbf{x}}_{Q_i}^{\mathrm{T}}\,\mathbf{F}_i\dot{\mathbf{q}}_{h_i} = \hat{\mathbf{x}}_{Q_i}^{\mathrm{T}}\,(\dot{\mathbf{x}}_{ol} + \mathbf{M}_i\dot{\mathbf{x}}_{oa}) \tag{43}$$

$$\hat{\mathbf{y}}_{Q_i}^{\mathrm{T}}\,\mathbf{F}_i\dot{\mathbf{q}}_{h_i} = \hat{\mathbf{y}}_{Q_i}^{\mathrm{T}}\,(\dot{\mathbf{x}}_{ol} + \mathbf{M}_i\dot{\mathbf{x}}_{oa}). \tag{44}$$

For convenience, vectors $\hat{\mathbf{x}}_{Q_i}$ and $\hat{\mathbf{y}}_{Q_i}$ are put in matrix form as $\mathbf{G}_i = [\hat{\mathbf{x}}_{Q_i}, \hat{\mathbf{y}}_{Q_i}]^{\mathrm{T}}$, and we define $\mathbf{P}_i = [\mathbf{I}_{3\times 3}, \mathbf{M}_i]$. As a reminder, these matrices are used to derive the overall Jacobian equation, as shown in (11).

ACKNOWLEDGMENT

The corresponding author acknowledges the clinical advice of Dr. J. Handa of the Johns Hopkins Eye Institute.

REFERENCES

[1] K. W. Grace, "Kinematic design of an ophthalmic surgery robot and feature extracting bilateral manipulation" Ph.D. dissertation, Dept. Mech. Eng., Northwestern Univ., Chicago, IL, 1995.

[2] H. Das, H. Zak, J. Johnson, J. Crouch, and D. Frambach, "Evaluation of a telerobotic system to assist surgeons in microsurgery," *Comput. Aided Surg.*, vol. 4, pp. 15–25, 1999.

[3] S. Charles, H. Das, T. Ohm, C. Boswell, G. Rodriguez, R. Steele, and D. Istrade, "Dexterity-enhanced telerobotic microsurgery," in *Proc. 8th Int. Conf. Adv. Robot.*, Monterey, CA, 1997, pp. 5–10.

[4] C. N. Riviere, W. T. Ang, and P. K. Khosla, "Toward active tremor canceling in handheld microsurgical instruments," *IEEE Trans. Robot. Autom.*, vol. 19, no. 5, pp. 793–800, Oct. 2003.

[5] R. Kumar, P. Berkelman, P. Gupta, A. Barnes, P. S. Jensen, L. L. Whitcomb, and R. H. Taylor, "Preliminary experiments in cooperative human/robot force control for robot assisted microsurgical manipulation," in *Proc. IEEE Int. Conf. Robot. Autom.*, San Francisco, CA, 2000, pp. 610–617.

[6] R. Taylor, P. Jensen, L. Whitcomb, A. Barnes, R. Kumar, D. Stoianovici, P. Gupta, Z. Wang, E deJuan, and L. Kavoussi, "Steady-hand robotic system for microsurgical augmentation," *Int. J. Robot. Res.*, vol. 18, pp. 1201–1210, 1999.

[7] K. Ikuta, T. Kato, and S. Nagata, "Development and experimental verification of micro active forceps for microsurgery," in *Proc. Int. Symp. Micromechatron. Human Sci.*, Nagoya, Japan, 1996, pp. 229–234.

[8] C. N. Riviere and P. S. Jensen, "A study of instrument motion in retinal microsurgery," in *Proc. Annu. Int. Conf. IEEE Eng. Med. Biol.*, Chicago, IL, 2000, pp. 59–60.

[9] S. P. N. Singh and C. N. Riviere, "Physiological tremor amplitude during retinal microsurgery," in *Proc. IEEE 28th Annu. Northeast Bioeng. Conf.*, Philadelphia, PA, 2002, pp. 171–172.

[10] A. Jagtap and C. Riviere, "Applied force during vitreoretinal microsurgery with handheld instruments," in *Proc. 26th Annu. Int. Conf. IEEE EMBS*, San Francisco, CA, 2004, pp. 2771–2773.

[11] W. Wei, R. Goldman, N. Simaan, H. Fine, and S. Chang, "Design and theoretical evaluation of micro-surgical manipulators for orbital manipulation and intraocular dexterity," in *Proc. IEEE Int. Conf. Robot. Autom.*, Rome, Italy, 2007, pp. 3389–3395.

[12] A. Bicchi, C. Melchiorri, and D. Balluchi, "On the manipulability of general multiple limb robots," *IEEE Trans. Robot. Autom.*, vol. 11, no. 2, pp. 215–228, Apr. 1995.

[13] A. Bicchi and D. Prattichizzo, "Manipulability of cooperating robots with unactuated and closed-chain mechanisms," *IEEE Trans. Robot. Autom.*, vol. 16, no. 4, pp. 336–345, Aug. 2000.

[14] S. Lee, "Dual redundant arm configuration optimization with task-oriented dual arm manipulability," *IEEE Trans Robot. Autom.*, vol. 5, no. 1, pp. 78–97, Feb. 1989.

[15] J. T.-Y. Wen and L. S. Wilfinger, "Kinematic manipulability of general constrained rigid multibody systems," *IEEE Trans. Robot. Autom.*, vol. 15, no. 3, pp. 558–567, Jun. 1999.

[16] G. Liu, J. Xu, X. Wang, and Z. Li, "On quality functions for grasp synthesis, fixture planning, and coordinated manipulation," *IEEE Trans. Robot. Autom.*, vol. 1, no. 2, pp. 146–162, Oct. 2004.

[17] R. M. Murray and S. S. Sastry, "Grasping and manipulation using multifingered robot hands," in *Proc. Symp. Appl. Math.*, Louisville, KY, 1990, pp. 91–127.

[18] Y. Nakamura, K. Nagai, and T. Yoshikawa, "Dynamics and stability in coordination of multiple robotic mechanisms," *Int. J. Robot. Res.*, vol. 8, pp. 44–61, 1989.

[19] P. Chiacchio, S. Chiaverini, L. Sciavicco, and B. Siciliano, "Global task space manipulability ellipsoids for multiple-arm systems," *IEEE Trans. Robot. Autom.*, vol. 7, no. 5, pp. 678–685, Oct. 1991.

[20] T. Yoshikawa, "Manipulability of robotic mechanisms," *Int. J. Robot. Res.*, vol. 4, pp. 3–9, 1985.

[21] R. Finotello, T. Grasso, G. Rossi, and A. Terribile, "Computation of kinetostatic performances of robot manipulators with polytopes," in *Proc. IEEE Int. Conf. Robot. Autom.*, Leuven, Belgium, 1998, pp. 3241–3246.

[22] J. Lee, "A study on the manipulability measures for robot manipulators," in *Proc IEEE/RSJ Int. Conf. Intell. Robot. Syst.*, Grenoble, France, 1997, pp. 1458–1465.

[23] J. Angeles, *Fundamentals of Robotic Mechanical Systems*, 2nd ed. New York: Springer-Verlag, 2002.

[24] A. Fattah and A. M. Hasan Ghasemi, "Isotropic design of spatial parallel manipulators," *Int. J. Robot. Res.*, vol. 21, pp. 811–824, 2002.

[25] J. Angeles and C. S. Lopez-Cajun, "Kinematic isotropy and the conditioning index of serial robotic manipulators," *Int. J. Robot. Res.*, vol. 11, pp. 560–571, 1992.

[26] C. M. Gosselin and J. Angeles, "A global performance index for the kinematic optimization of robotic manipulators," *ASME J. Mech. Design*, vol. 113, pp. 220–226, 1991.

[27] J.-P. Merlet, "Jacobian, manipulability, condition number, and accuracy of parallel robots," *ASME J. Mech. Des.*, vol. 128, pp. 199–206, 2006.

[28] C. Gosselin, "The optimum design of robotic manipulators using dexterity indices," *Robot. Auton. Syst.*, vol. 9, pp. 213–226, 1992.

[29] F. Park and R. Brockett, "Kinematic dexterity of robotic mechanisms," *Int. J. Robot. Res.*, vol. 13, pp. 1–15, 1994.

[30] Y. Wang and G. S. Chirikjian, "Propagation of errors in hybrid manipulators," in *Proc. 2006 IEEE Int. Conf. Robot. Autom.*, Orlando, FL, pp. 1848–1853.
[31] D. Albert and M. Lucarelli, *Clinical Atlas Procedures in Ophthalmic Surgery*. Atlanta, GA: AMA, 2004.
[32] S. Okazawa, R. Ebrahimi, J. Chuang, S. E. Salcudean, and R. Rohling, "Hand-held steerable needle device," *IEEE/ASME Trans. Mechatron.*, vol. 10, no. 3, pp. 285–296, Jun. 2005.
[33] R. J. Webster, A. M. Okamura, and N. J. Cowan, "Toward active cannulas: Miniature snake-like surgical robots," in *Proc. 2006 IEEE/RS*, Beijing, China, pp. 2857–2863.
[34] D. Stewart, "A platform with 6 degrees of freedom," *Proc. Inst. Mech. Eng.*, vol. 180, no. 15, pp. 371–386, 1965.
[35] G. Brandt, K. Radermacher, S. Lavallee, H.-W. Staudte, and G. Rau, "A compact robot for image guided orthopedic surgery: Concept and preliminary results," in *Lecture Notes in Computer Science (LNCS)*, vol. 1205, J. Troccaz, E. Grimson, and R. Mosges, Eds. Berlin, Germany: Springer-Verlag, 1997, pp. 767–776.
[36] M. Shoham, M. Burman, E. Zehavi, L. Joskowicz, E. Batkilin, and Y. Kunicher, "Bone-mounted miniature robot for surgical procedures: Concept and clinical applications," *IEEE Trans. Robot. Autom.*, vol. 19, no. 5, pp. 893–901, Oct. 2003.
[37] N. Simaan, "Analysis and synthesis of parallel robots for medical applications," M.Sc. thesis, Dept. Mech. Eng., Technion—Israel Inst. Technol. Haifa, Isarel, 1999.
[38] A. Wolf and B. Jaramaz, "MBARS: Mini bone attached robotic system for joint arthroplasty," in *Proc. 1st IEEE/RAS—EMBS Int. Conf. Biomed. Robot. Biomechatron.*, Pisa, Italy, 2006, pp. 1053–1058.
[39] M. Wapler, V. Urban, T. Weisener, J. Stalkamp, M. Durr, and A. Hiller, "A Stewart platform for precision surgery," *Trans. Inst. Meas. Control*, vol. 24, pp. 329–334, 2003.
[40] J.-P. Merlet, "Singular configurations of parallel manipulators and grassmann geometry," *Int. J. Robot. Res.*, vol. 8, pp. 45–56, 1989.
[41] L.-W. Tsai, *Robot Analysis: The Mechanics Serial Parallel Manipulators*. Hoboken, NJ: Wiley, 1999.
[42] J.-P. Merlet, *Parallel Robots*, 2nd ed. Dordrecht, The Netherlands: Springer-Verlag, 2006.
[43] H. Lipkin and J. Duffy, "Hybrid twist and wrench control for a robotic manipulator," *ASME J. Mech. Design*, vol. 110, pp. 138–144, 1988.
[44] L. J. Stocco, S. E. Salcudean, and F. Sassani, "On the use of scaling matrices for task-specific robot design," *IEEE Trans. Robot. Autom.*, vol. 15, no. 5, pp. 958–965, Oct. 1999.
[45] Y. Nakamura, *Advanced Robotics Redundancy and Optimization*, 1st ed. Boston, MA: Addison-Wesley, 1991.

Wei Wei (S'06) received the B.Eng. degree from Tsinghua University, Beijing, China, in 2003, the M.Eng. degree from McGill University, Montreal, QC, Canada, in 2005, and the M.Phil. degree from Columbia University, New York, NY, in 2007, all in mechanical engineering. He is currently working toward the Ph.D. degree with the Department of Mechanical Engineering, Columbia University.

His current research interests include parallel robots, flexible robots, medical robotics, mechanical system synthesis, and control systems.

Roger E. Goldman received the B.Sc. degree in mechanical engineering from Stanford University, Stanford, CA, in 2002. He is currently working toward the M.D. and Ph.D. degrees in biomedical engineering at Columbia University, New York, NY.

In 2003, he joined Foxhollow Technologies, Inc., Redwood City, CA, where he developed catheters for endovascular procedures. He is currently a National Institutes of Health (NIH) Medical Scientist Training Program Fellow at Columbia University. His current research interests include novel robotic instruments for applications in medical diagnosis and therapy.

Howard F. Fine received the B.S. degree in chemical engineering and biology from the Massachusetts Institute of Technology, Cambridge, in 1996, the M.D. (*cum laude*) degree from Harvard Medical School, Boston, MA, in 2001, and the M.H.Sc. degree in clinical trials from Duke University Medical Center, Durham, NC, in 2000.

In 2005, he completed the Ophthalmology Residency at Wilmer Eye Institute, Johns Hopkins Medical Institutes, Baltimore, MD, and, in 2007, the fellowship training in vitreoretinal surgery from Edward S. Harkness Eye Institute, Columbia University Medical Center, New York, NY, where he is currently the Medical Director of the Gerstner Clinical Research Center and an Assistant Professor of ophthalmology. He has authored or coauthored literature on minimally invasive vitreoretinal surgical outcomes, autofluorescence imaging of the retina, and the use of monoclonal antibodies in the treatment of retinal vascular diseases. His current research interests include expanding vitreoretinal surgical capabilities, retinal imaging, and novel therapeutics for retinal vascular disease.

Stanley Chang received the B.S. degree in electrical engineering from the Massachusetts Institute of Technology, Cambridge, in 1968, the M.S. degree in biomedical engineering from the University of Pennsylvania, Philadelphia, in 1970, and the M.D. degree from Columbia University College of Physicians and Surgeons, New York, NY, in 1974.

In 1978, he completed the residency in ophthalmology at the Massachusetts Eye and Ear Infirmary, Harvard Medical School and, in 1979, the fellowship in vitreoretinal surgery at Bascom Palmer Eye Institute, University of Miami, Miami, FL. He is currently the Chairman of the Department of Ophthalmology, Edward S. Harkness Eye Institute, Columbia University College of Physicians and Surgeons. He pioneered the use of wide-angle visualization systems for vitreoretinal surgery and heavy liquids for the treatment of complex retinal detachments, including giant retinal tears. His current research interests include vitreoretinal surgical instrumentation, novel tamponade agents for complex retinal detachment, and the genetics of and gene therapy for heritable retinal conditions.

Dr. Chang is considered one of the world's foremost vitreoretinal surgeons and was named the Physician of the Year nationwide in 2008 by Castle Connolly, Inc.

Nabil Simaan (M'03) received the B.Sc., M.Sc., and Ph.D. degrees in mechanical engineering from Technion—Israel Institute of Technology, Haifa, Israel, in 1996, 1999, and 2002, respectively.

His Masters and Ph.D. research focused on the design, synthesis, and singularity analysis of parallel robots for medical applications, stiffness synthesis, and modulation for parallel robots with actuation and kinematic redundancies. In 2003, he was a Postdoctoral Research Scientist at Johns Hopkins University National Science Foundation (NSF) Engineering Research Center for Computer-Integrated Surgical Systems and Technology (ERC-CISST), Baltimore, MD, where he focused on minimally invasive robotic assistance in confined spaces. In 2005, he joined Columbia University, New York, NY, as an Assistant Professor of mechanical engineering and the Director of the Advanced Robotics and Mechanisms Applications (ARMA) Laboratory. During the course of his research, he designed and constructed compact parallel robots for medical applications and compact and downscalable surgical slaves for minimally invasive surgery of the throat and upper airway. His current research interests include synthesis of novel robotic systems for surgical assistance in confined spaces with applications to minimally invasive surgery of the throat, natural orifice surgery, cochlear implant surgery, and dexterous bimanual microsurgery.